

One-dimensional radiation-hydrodynamic simulations of imploding spherical plasma liners with detailed equation-of-state modeling

J. S. Davis,^{1, a)} S. C. Hsu,^{1, b)} I. E. Golovkin,² J. J. MacFarlane,² and J. T. Cassibry³

¹⁾*Physics Division, Los Alamos National Laboratory, Los Alamos, NM 87545*

²⁾*Prism Computational Sciences, Inc., Madison, WI 53711*

³⁾*Propulsion Research Center, University of Alabama in Huntsville, Huntsville, AL 35899*

(Dated: 5 September 2018)

This work extends the one-dimensional radiation-hydrodynamic imploding spherical argon plasma liner simulations of T. J. Awe *et al.* [Phys. Plasmas **18**, 072705 (2011)] by using a detailed tabular equation-of-state (EOS) model, whereas Awe *et al.* used a polytropic EOS model. Results using the tabular EOS model give lower stagnation pressures by a factor of 3.9–8.6 and lower peak ion temperatures compared to the polytropic EOS results. Both local thermodynamic equilibrium (LTE) and non-LTE EOS models were used in this work, giving similar results on stagnation pressure. The lower stagnation pressures using a tabular EOS model are attributed to a reduction in the liner's ability to compress arising from the energy sink introduced by ionization and electron excitation, which are not accounted for in a polytropic EOS model. Variation of the plasma liner species for the same initial liner geometry, mass density, and velocity was also explored using the LTE tabular EOS model, showing that the highest stagnation pressure is achieved with the highest atomic mass species for the constraints imposed.

^{a)}Now at Applied Physics, University of Michigan, Ann Arbor, MI 48109

^{b)}Email: scotthsu@lanl.gov

I. INTRODUCTION

The Plasma Liner Experiment (PLX) at Los Alamos National Laboratory was designed to form and study spherically imploding plasma liners via the merging of thirty supersonic plasma jets.¹ Such imploding plasma liners could potentially allow repetitive generation of cm-, μ s-, and Mbar-scale plasmas for fundamental high energy density plasma physics studies, or (if scaled up in energy) be used as a standoff compression driver¹⁻³ for magneto-inertial fusion (MIF).⁴⁻⁶ Recent one-dimensional (1D) radiation-hydrodynamic simulations of targetless imploding spherical argon plasma liners by Awe *et al.*⁷ used a polytropic equation-of-state (EOS) model, providing insight into the 1D physical evolution of imploding spherical plasma liners, and showing that PLX-relevant plasma liner kinetic energies of hundreds of kJ could result in liner stagnation pressures on the order of 1 Mbar sustained for order 1 μ s. The results of Awe *et al.*⁷ indicated high enough plasma temperatures (10's of eV) for ionization effects, which are not included in a polytropic EOS model, to have an appreciable impact on both the predicted peak pressures and temperatures. As some of the initial liner kinetic energy would now be used for ionization, it is expected that the liner may compress less, although the expected drop in thermal energy in the imploding plasma liner due to ionization and radiative loss channels are expected to help compensate. Note that this work and that of Awe *et al.*⁷ focus on targetless, self-collapse of the liner, motivated by the goals of the PLX project. Thus, care must be taken in using these results to provide insight into plasma liner implosions onto a magnetized target for MIF, which has been explored in several other recent publications.⁸⁻¹¹

The purpose of this work is to develop insight into how a detailed EOS model, and particularly ionization, affect spherically symmetric, targetless plasma liner implosions. We used the HELIOS-CR¹² 1D radiation-hydrodynamic code and the PROPACEOS¹² EOS and multi-group opacity database to repeat the simulation cases presented in Awe *et al.*⁷ In particular, we examined how the detailed EOS model affected the liner stagnation pressure P_{stag} (defined in Sec. II C), the stagnation time τ_{stag} (defined in Sec. II C), the implosion trajectory and minimum radius achieved, and scaling behavior of P_{stag} as a function of initial plasma liner parameters. In all cases, we used argon as did Awe *et al.*⁷ However, for a particular initial liner geometry, mass density, and velocity (corresponding to an initial energy of 375 kJ, relevant for PLX), we also ran simulations using H, D-T, ⁴He, ⁶Li, ¹¹B, Ne,

Kr, and Xe, in addition to Ar. In this work, as in Awe *et al.*,⁷ we set aside the important issues of 3D effects of the discrete merging plasma jets and 3D convergent instabilities such as Rayleigh-Taylor and others, which are addressed elsewhere,¹³ and study spherically symmetric imploding plasma liners initiated at a jet merging radius R_m at which plasma jets are assumed to have merged.

The remainder of the paper is organized as follows. Sec. II describes our modeling approach including the choice of liner initial conditions investigated, details of the codes used, and benchmarking against the results of Awe *et al.*⁷ Section III presents the new simulation results including (1) comparison of results using local thermodynamic equilibrium (LTE) versus non-LTE EOS tables, (2) comparison of plasma liner implosions using a LTE tabular EOS versus a polytropic EOS, (3) P_{stag} scaling with initial liner density and velocity, and (4) different plasma species for one liner initial condition. Section IV provides a discussion and summary.

II. MODELING APPROACH

In this section we describe the simulation initial conditions, the codes used, and benchmarking of our own polytropic EOS results against the results of Awe *et al.*⁷

A. Simulation initial conditions

The initial conditions used in this work are shown schematically in Fig. 1 and summarized in Table I (columns 2–5). The rationale for these choices are described in detail in Awe *et al.*⁷ In short, they are intended to span a range of initial plasma liner velocities v_0 and kinetic energies KE_0 from PLX-relevant values (50 km/s, hundreds of kJ) at the lower end to what might be needed for an MIF standoff compression driver^{1–3} (> 50 km/s, $>$ tens of MJ) at the higher end. The initial liner ion density values n_0 are what can be expected based on plasma jet densities that have already been achieved by the plasma guns designed and built by HyperV Technologies¹⁴ for use on PLX. In this work, we assume that discrete plasma jets have merged at $R_m = 24.1$ cm and formed a spherically symmetric imploding plasma liner with uniform mass density ρ_0 , thickness 25.5 cm, temperature $T_0 = T_e = T_i = 1.0$ eV, and uniform inward radial velocity v_0 . The effects of non-uniform initial liner profiles are not

studied here but are a potential way of optimizing imploding plasma liner performance.¹⁵ The void region (Fig. 1) is modeled using very low density plasma with mass densities of 10^{-8} kg/m³ (tabular EOS runs) and 10^{-9} kg/m³ (polytropic EOS runs), temperature of 1.0 eV, and the same species as the liner. The different initial void mass densities led to slightly different computational zone setups but did not affect the overall liner evolution.

Although this work does not focus on the physical evolution of a spherical plasma liner imploding on vacuum, which was described in detail in Awe *et al.*,⁷ we provide here a brief summary of its 1D evolution: (1) the imploding liner converges toward the origin, and the liner density rises as R^{-2} , (2) upon the liner reaching the origin, an outward going shock propagates radially outward, shock-heating the incoming liner material, and (3) the outgoing shock reaches the outer edge of the incoming liner, at which time the high pressure of the post-shocked liner material can no longer be sustained, and the entire system disassembles.

B. Computational codes

This work used the HELIOS-CR¹² 1D radiation-hydrodynamic code with LTE and non-LTE EOS tables generated using the PROPACEOS¹² code. HELIOS-CR is a Lagrangian code that can use both a polytropic EOS (with adiabatic constant γ) or a tabular EOS. The HELIOS-CR code has been applied previously to the modeling of inertial confinement fusion (ICF) implosions.^{16,17} PROPACEOS EOS and frequency-dependent opacities are computed using a combination of an isolated atom model and, at high densities at which cohesive effects are important, a quotidian-EOS-like model.¹⁸ At the densities of interest in this paper, energies and pressures are computed for an isolated atom model in which atomic level populations are computed using Boltzmann statistics and the Saha equation (LTE case) or a collisional-radiative model (non-LTE case). The energies and pressures of the EOS tables are based on the free energy, thus providing for thermodynamically consistent energy and pressure values. For the non-LTE case, the effects of photoionization and photoexcitation are ignored when computing the temperature- and density- dependent tabular EOS data, as the radiation field is a non-local quantity, *i.e.*, the radiation can originate in other parts of the plasma, and therefore is unknown when generating the tables. Detailed atomic models are utilized in which all ionization stages are included, *e.g.*, for Ar, a total of $> 10^4$ energy levels are included. More than 10^6 transitions were used for the opacity calculations. Frequency-

dependent radiation transport is treated using a radiation diffusion model; fifty frequency groups were used in this work. When modeling a plasma that is not optically thick (our case) with radiation diffusion, it is possible that radiation losses could be overestimated. Finally, we checked energy conservation at $t = 5 \mu\text{s}$ (near peak compression) for the polytropic, LTE tabular, and non-LTE tabular cases, using run 6 of Table I as an example. Energy is conserved to within 0.1%, 0.1%, and 1.1% for the polytropic, LTE, and non-LTE runs, respectively. These are very small effects compared to the differences we report in this paper, and thus we conclude that energy conservation does not impact our results.

We previously verified⁷ a HELIOS-CR calculation against the convergent shock Noh problem¹⁹ and got better than 5% agreement for the highest resolution case we ran (50 μm zone resolution over a sphere with 25 cm initial radius). We also did a grid resolution convergence study showing that an average grid resolution of 250 μm gave $\sim 10\%$ accuracy.⁷ In this work, we used 400 computational zones over the initially 255 mm thick liner (average of 637.5 $\mu\text{m}/\text{zone}$), which was chosen based on achieving a balance between getting reasonable agreement in the benchmarking studies described in Sec. II C and the run time of each simulation (typically a few hours to a day per run). We used the automatic zoning feature of HELIOS-CR, and thus the zone size was much smaller than the average near boundaries and much larger elsewhere.

When using a polytropic EOS, HELIOS-CR only allows use of a one-temperature (1T) model. The tabular EOS simulations allow for separate ion T_i and electron T_e temperatures. All reported HELIOS-CR results with polytropic EOS are 1T, and all reported results with tabular EOS are 2T with radiation diffusion. To verify that the use of 1T versus 2T does not have a great impact on our results, we compared the time evolution of T_e and T_i for the zone initially at $R = 25.1 \text{ cm}$ and saw no difference. Furthermore, the T_i evolution from a 1T run was virtually the same as that from the 2T run.

C. Benchmarking against results of Awe *et al.*

Because Awe *et al.*⁷ used the 1D Lagrangian radiation-hydrodynamics code RAVEN,²⁰ we first benchmarked HELIOS-CR against RAVEN by performing runs 1–8 of Table I using a polytropic EOS and comparing with the RAVEN results. In this paper, all polytropic EOS runs used $\gamma = 1.6667$. We also included thermal transport and radiation diffusion to be

as consistent as possible with Awe *et al.*,⁷ which found that in these spherically convergent simulations, non-physical temperature and pressure spikes occur near the origin due to compression of the leading edge material of the liner. Including thermal and radiation transport in the simulations helps prevent these non-physical spikes, which prevent the imploding plasma liner from reaching as small a radius as it otherwise would, leading to a much-reduced peak pressure.⁷

We compared the quantities P_{stag} and τ_{stag} , where P_{stag} is defined as the thermal pressure in the simulation zone that is initially 1.0 mm from the inner edge of the liner ($R = 24.2$ cm) averaged over a time duration τ_{stag} , which is defined (and also shown graphically in Fig. 2A) as the time duration between maximum pressure to the time when pressure sustainment ends due to the outward going shock reaching the outer edge of the incoming liner. We found that RAVEN P_{stag} results (Table II) are 1.2–3.5 times higher than the HELIOS-CR results (Table III). The τ_{stag} results agree to within 20%. These differences were considered to be small enough to proceed with this study.

We also compared HELIOS-CR and RAVEN simulation results for the time evolution (Fig. 2A) of the pressure P , mass density ρ , and ion temperature T_i of a single computational zone (initially 1.0 cm from the inner edge of the liner, to be consistent with Fig. 4 of Awe *et al.*⁷), and the radial profiles (Fig. 2B) of P , ρ , and electron temperature T_e at a single time ($t = 6.5 \mu\text{s}$), for run 6 of Table I. Both comparisons indicate good qualitative agreement with some discrepancies. One difference is the increase in both P and T_i near the end of τ_{stag} for the HELIOS-CR but not the RAVEN results. The magnitude of the rise in P increases with increasing v_0 and is present throughout the entire stagnated liner, and is thus not a localized numerical effect in a single zone. The reason for this rise is not yet understood, but because this does not affect the conclusions of this paper, we have set the issue aside. There are also differences in the radial profiles at $t = 6.5 \mu\text{s}$, largely due to the slight difference in time evolution between the two simulations. At this time, there is an outward going shock for both the HELIOS-CR (at ~ 0.6 cm) and RAVEN (at ~ 0.5 cm) simulations, but the HELIOS-CR shock has propagated farther outward. The discrepancy in T_e inside the shock also appears to be due to the difference in time evolution, as slightly later radial profiles from the RAVEN results also fall toward the origin (see Fig. 4 of Awe *et al.*⁷). These differences do not affect the conclusions of this paper. The rest of the paper focuses on comparing HELIOS-CR simulations using a polytropic EOS versus tabular EOS data.

III. RESULTS

This section presents HELIOS-CR simulation results and analysis. Firstly, we discuss LTE versus non-LTE tabular EOS results, showing that there are only minor differences, thus justifying our choice to focus on the use of LTE for the subsequent results in the paper. Secondly, we compare argon plasma liner implosions between polytropic and a LTE tabular EOS to assess the effects of ionization and a more sophisticated treatment of EOS. Finally, we explore the effects of using different plasma liner species for run 6 of Table I, again using LTE tabular EOS data.

A. LTE versus Non-LTE EOS tabular data

The initial conditions we used (see Table I) are in a parameter space in which LTE is not obviously correct. Non-LTE can have an effect on EOS (*i.e.*, ionization/excitation) and radiation losses (excited states tend to be less populated). Below an argon ion density of $\sim 10^{17} \text{ cm}^{-3}$ at $\sim 1 \text{ eV}$, the fractions of Ar I, Ar II, and Ar III as a function of temperature are noticeably different between LTE and non-LTE calculations. Above $\sim 10^{17} \text{ cm}^{-3}$, corresponding to later stages of liner implosion and stagnation, the EOS data are similar. We performed run 6 of Table I using both LTE and non-LTE tabular EOS data to explicitly assess the difference in results. Figure 3 shows a comparison of P , ρ , and T_i versus time for the computational zone that is initially 1.0 cm from the inside edge of the plasma liner. Note that for the tabular EOS runs, the pressure is calculated as $n_i T_i + n_e T_e$, where n_i and n_e are the ion and electron densities, respectively, $n_e = Z n_i$, and Z is the mean charge state. The LTE and non-LTE results are virtually indistinguishable over the entire duration of the simulation, and there are also no appreciable differences in P , ρ , and T over the entire liner at several time steps (not shown). This indicates that either LTE or non-LTE EOS models could be used without altering the relevant simulation results for the purposes of this study, and thus we used LTE for all subsequent results presented in the paper.

B. Tabular LTE EOS versus polytropic EOS

To assess the effects of ionization and other effects included in the LTE tabular EOS data, we compared HELIOS-CR simulation results using LTE tabular EOS with those using

a polytropic ($\gamma = 1.6667$) EOS for runs 1–8 of Table I. For the computational zone that is initially 1.0 mm from the inside edge of the liner, the maximum pressure P_{max} is 3.6–6.1 times larger and P_{stag} 3.9–8.6 times larger for the polytropic EOS results. Complete results for both the tabular LTE and polytropic EOS’s are shown in Tables I and III, respectively. The T_i and ρ at peak compression were also higher in the polytropic EOS results as well (not shown). Figure 4 shows P , ρ , T_i , and radial position versus time of the computational zone initially at 25.1 cm (1.0 cm from the inside edge of the liner) for the initial conditions of run 6 of Table I. The lower P_{max} (\sim zone thermal energy divided by zone volume) for the tabular EOS result is consistent with the combined effects of lower zone thermal energy ($\sim \rho T$) and higher zone volume at peak compression, as compared to the polytropic result. Next, we investigate in more detail the reasons for the lower zone thermal energy and higher zone volume at peak compression for the tabular EOS run.

Figure 5 shows various components of the total liner energy versus time for run 6 of Table I. The liner kinetic energy KE falls quickly around 5 μ s when the leading edge of the liner reaches peak compression and stagnates. In the polytropic EOS case, the difference between the initial KE and the stagnated liner thermal energy TE is due mostly to radiative losses. In the tabular EOS case, around half of the initial liner KE goes to ionization/excitation energy, which is stored in free and excited electrons in the stagnated liner. The mean charge peaks around 7 (see Sec. III D). The result of including the ionization/excitation physics is a drastic reduction in the liner compression at stagnation, leading to lower P_{stag} (see Tables I and III).

C. Stagnation pressure scalings

Awe *et al.*⁷ found the approximate scalings $P_{stag} \sim v_0^{15/4}$ and $P_{stag} \sim n_0^{1/2}$ for the cases in Table I using a polytropic EOS model, and gave an heuristic argument for why $P_{stag} \sim v_0^5$ ought to be an upper bound on the scaling dependence of P_{stag} on v_0 . The heuristic argument invoked the following assumptions: (1) perfect conversion of liner KE to liner TE at stagnation, (2) no radiation and thermal losses, and (3) no entropy production due to the outward going post-stagnation shock. Because the RAVEN runs of Awe *et al.*⁷ included radiation and thermal losses, the observed weaker $P_{stag} \sim v_0^{15/4}$ scaling is consistent with the heuristic upper bound of $P_{stag} \sim v_0^5$. Our HELIOS-CR runs using a LTE tabular EOS violate

assumption (1) above due to the major ionization/excitation energy channel discussed in Sec. III B. Thus, it is expected we should see an even weaker scaling than $P_{stag} \sim v_0^{15/4}$.

Figure 6 shows P_{stag} versus n_0 and v_0 and fits to power law functions for HELIOS-CR simulations of the cases in Table I using a LTE tabular EOS model. While the fitted exponents are very similar across density and velocity groups in Awe *et al.*,⁷ *i.e.*, $P_{stag} \sim n_0^{0.54 \pm 0.02}$ and $P_{stag} \sim v_0^{3.71 \pm 0.08}$, our fitted exponents have a much wider spread, *i.e.*, $P_{stag} \sim n_0^{0.64 \pm 0.14}$ and $P_{stag} \sim v_0^{2.91 \pm 0.30}$. This larger spread in exponents is likely due to the fact that the LTE tabular EOS is sensitive to density and temperature in the imploding plasma liner, thus introducing a degree of variability that depends on the liner initial conditions not expected in the polytropic EOS simulations of Awe *et al.*⁷ Our $P_{stag} \sim v_0^{2.91 \pm 0.30}$ scaling (depending on n_0) is indeed weaker than the approximate $P_{stag} \sim v_0^{15/4}$ scaling of Awe *et al.*,⁷ as expected. Our $P_{stag} \sim n_0^{0.64 \pm 0.14}$ scaling agrees with the $P_{stag} \sim n_0^{1/2}$ scaling of Awe *et al.*⁷ within our observed variation across velocity groups.

D. Varying the liner species

Due to the significant effect of ionization/excitation on achievable P_{stag} , we explored the use of different plasma species for the same initial liner ρ_0 and v_0 (and hence KE) of run 6 of Table I. The only quantity that was varied was the initial number density n_0 to keep ρ_0 constant. We performed HELIOS-CR simulations with LTE tabular EOS data to investigate the effect of species on P_{stag} . The species chosen for study are those of interest as fusion fuel, blanket materials, or MIF implosion drivers for fusion energy applications: H, D-T (50%-50% by atom), ⁴He, ⁶Li, ¹¹B, Ne, Ar, Kr, and Xe.

Figure 7A shows HELIOS-CR simulation results using a LTE tabular EOS model for P , volume, TE , and ionization/excitation energy at peak compression versus atomic mass number for the zone initially 1.0 cm from the inner edge of the liner. There is a clear trend of increasing peak P with atomic mass number, quantitatively consistent with the combined effects of decreasing volume and thermal pressure with atomic mass number at peak compression. The thermal and ionization/excitation energies are not monotonic with atomic mass number, and this is related to the different atomic and radiative properties of the different species.

We also examined the mean charge and electron count versus time (Fig. 7B) for the same

computational zone as above. Although the heavier species have more electrons to ionize, there are a larger number of the lighter species present by the ratio of their atomic mass numbers. It turns out that the peak mean charge for the heavier species reaches only about 5–10 (Fig. 7B), much less than the mass ratios between the heavier and lighter species, and thus the electron count is higher for the lighter species. Thus, the ionization/excitation energies are in general higher for the lighter species, in part explaining why they reach lower peak pressures for the initial conditions imposed.

IV. DISCUSSION AND SUMMARY

It appears that the key effect of using a LTE tabular EOS rather than a polytropic EOS is the significant diversion of liner KE into ionization/excitation, which is not included in the polytropic EOS model. The diversion of initial liner KE leads to less effective compression, larger minimum volume at peak compression, and thus lower P_{stag} which is inversely proportional to volume. This is detrimental for reaching very high peak temperatures and pressures in targetless spherical plasma liner implosions, which was one of the design objectives of PLX. For a given initial liner KE , which is a natural experimental constraint, the results suggest the use of lower density and higher velocity to achieve higher peak pressure. The previous statement is confirmed by examining, *e.g.*, the P_{stag} results from runs 3, 6, and 9 (375 kJ), or runs 4, 7, 10, and 13 (1.5 MJ) of Table I. Higher velocity should also be coupled with the use of lower atomic mass number species so as to fully strip the ions and eliminate the ionization/excitation and line radiation energy channels beyond a certain point in the implosion, after which the liner KE will predominantly go toward stagnation thermal pressure. This is in apparent contradiction with the results of Sec. III D, which suggest the use of heavier species for higher P_{stag} but only because we constrained the species comparison study by enforcing the same v_0 and ρ_0 . In our species comparison study, the much higher n_0 of the lighter species leads to more of the initial liner KE going into ionization/excitation. Further study is needed for optimizing P_{stag} in targetless spherical plasma liner implosions for a given initial liner KE .

The above discussion does not apply for the MIF application of a plasma liner compressing a magnetized D-T target plasma.¹ In that case, the imploding plasma liner is intended to be only a pusher that should complete its job of compressing the D-T target to fusion

conditions before the liner itself has a chance to get significantly compressed and heated. Thus, for initial liner n_0 and v_0 that are likely to be limited by available plasma gun technology, the MIF application likely will prefer a heavy liner species (to maximize ρv^2) since the ionization/excitation should not matter until after the D-T target has reached peak compression.

In summary, we have presented new 1D HELIOS-CR radiation-hydrodynamic simulation results of spherical plasma liners imploding on vacuum using a LTE tabular EOS model. The results were compared in detail to HELIOS-CR simulations using a polytropic EOS model ($\gamma = 1.6667$), which in turn were benchmarked against the polytropic EOS simulation results of Awe *et al.*⁷ We found that the liner stagnation pressure P_{stag} is lower by a factor of 3.9–8.6 using the LTE tabular EOS model. This is attributed to a significant amount of the initial liner kinetic energy going toward ionization/excitation of the plasma liner, resulting in less effective compression of the liner. We also studied the effect of different species on P_{stag} for the same initial liner geometry, mass density, and velocity. We found that with these constraints, the heaviest species reach the highest values of P_{stag} . This is attributed to less total energy going to ionization/excitation due to a smaller value at peak compression of the liner mean charge times the initial number density.

ACKNOWLEDGMENTS

The authors thank T. J. Awe for access to the RAVEN simulation data. This work was supported by the Office of Fusion Energy Sciences of the U.S. Department of Energy.

REFERENCES

- ¹S. C. Hsu, T. J. Awe, S. Brockington, A. Case, J. T. Cassibry, G. Kagan, S. J. Messer, M. Stanic, X. Tang, D. R. Welch, and F. D. Witherspoon, *IEEE Trans. Plasma Sci.* **40**, 1287 (2012).
- ²Y. C. F. Thio, E. Panarella, R. C. Kirkpatrick, C. E. Knapp, F. Wysocki, P. Parks, and G. Schmidt, in *Current Trends in International Fusion Research—Proceedings of the Second International Symposium*, edited by E. Panarella (National Research Council of Canada, Ottawa, 1999).

- ³Y. C. F. Thio, C. E. Knapp, R. C. Kirkpatrick, R. E. Siemon, and P. J. Turchi, *J. Fusion Energy* **20**, 1 (2001).
- ⁴I. R. Lindemuth and R. C. Kirkpatrick, *Nucl. Fusion* **23**, 263 (1983).
- ⁵R. C. Kirkpatrick, I. R. Lindemuth, and M. S. Ward, *Fusion Tech.* **27**, 201 (1995).
- ⁶I. R. Lindemuth and R. E. Siemon, *Amer. J. Phys.* **77**, 407 (2009).
- ⁷T. J. Awe, C. S. Adams, J. S. Davis, D. S. Hanna, S. C. Hsu, and J. T. Cassibry, *Phys. Plasmas* **18**, 072705 (2011).
- ⁸P. B. Parks, *Phys. Plasmas* **15**, 062506 (2008).
- ⁹J. T. Cassibry, R. J. Cortez, S. C. Hsu, and F. D. Witherspoon, *Phys. Plasmas* **16**, 112707 (2009).
- ¹⁰R. Samulyak, P. Parks, and L. Wu, *Phys. Plasmas* **17**, 092702 (2010).
- ¹¹J. F. Santarius, *Phys. Plasmas* **19**, 072705 (2012).
- ¹²J. J. MacFarlane, I. E. Golovkin, and P. R. Woodruff, *J. Quant. Spect. Rad. Transfer* **99**, 381 (2006).
- ¹³J. T. Cassibry, M. Stanic, S. C. Hsu, F. D. Witherspoon, and S. I. Abarzhi, *Phys. Plasmas* **19**, 052702 (2012).
- ¹⁴F. D. Witherspoon, S. Brockington, A. Case, S. J. Messer, L. Wu, R. Elton, S. C. Hsu, J. T. Cassibry, and M. A. Gilmore, *Bull. Amer. Phys. Soc.* **56**, 311 (2011).
- ¹⁵G. Kagan, X. Tang, S. C. Hsu, and T. J. Awe, *Phys. Plasmas* **18**, 120702 (2011).
- ¹⁶J. J. MacFarlane, I. E. Golovkin, R. C. Mancini, L. A. Welser, J. E. Bailey, J. A. Koch, T. A. Mehlhorn, G. A. Rochau, P. Wang, and P. Woodruff, *Phys. Rev. E* **72**, 066403 (2005).
- ¹⁷L. Welser-Sherrill, R. C. Mancini, J. A. Koch, N. Izumi, R. Tommasini, S. W. Haan, D. A. Haynes, I. E. Golovkin, J. J. MacFarlane, J. A. Delettrez, F. J. Marshall, S. P. Regan, V. A. Smalyuk, and G. Kyrala, *Phys. Rev. E* **76**, 056403 (2007).
- ¹⁸R. M. More, K. H. Warren, D. A. Young, and G. B. Zimmerman, *Phys. Fluids* **31**, 3059 (1988).
- ¹⁹W. F. Noh, *J. Comp. Phys.* **72**, 78 (1987).
- ²⁰T. A. Oliphant, "RAVEN Physics Manual," Tech. Rep. LA-8802-M (Los Alamos National Laboratory, NM, 1981).

Run	n_0 (cm ⁻³)	ρ_o (kg/m ³)	v_0 (km/s)	KE_0 (J)	τ_{stag} (μ s)	P_{stag} (Pa)	P_{max} (Pa)	$P_{stag}\tau_{stag}$	$P_{stag}\tau_{stag}/KE_0$
1	2.5E+15	1.66E-4	25	2.35E+4	9.40	4.49E+07	1.31E+08	4.22E+2	0.018
2	2.5E+15	1.66E-4	50	9.39E+4	5.35	3.54E+08	1.84E+09	1.90E+3	0.020
3	2.5E+15	1.66E-4	100	3.76E+5	2.70	3.93E+09	1.43E+10	1.06E+4	0.028
4	2.5E+15	1.66E-4	200	1.50E+6	1.30	2.84E+10	5.69E+10	3.69E+4	0.025
5	1.0E+16	6.63E-4	25	9.38E+4	9.55	9.15E+07	3.57E+08	8.74E+2	0.093
6	1.0E+16	6.63E-4	50	3.75E+5	5.35	6.43E+08	4.63E+09	3.44E+3	0.092
7	1.0E+16	6.63E-4	100	1.50E+6	2.70	8.20E+09	3.13E+10	2.21E+4	0.015
8	1.0E+16	6.63E-4	200	6.00E+6	1.35	5.70E+10	1.26E+11	7.40E+4	0.013
9	4.0E+16	2.65E-3	25	3.75E+5	10.45	3.47E+08	1.43E+09	3.62E+3	0.010
10	4.0E+16	2.65E-3	50	1.50E+6	5.45	2.00E+09	1.43E+10	1.09E+4	0.007
11	4.0E+16	2.65E-3	100	6.00E+6	2.70	1.79E+10	1.30E+11	4.83E+4	0.008
12	4.0E+16	2.65E-3	200	2.40E+7	1.35	1.13E+11	7.39E+11	1.53E+5	0.006
13	1.6E+17	1.06E-2	25	1.50E+6	10.50	1.23E+09	4.97E+09	1.29E+4	0.009
14	1.6E+17	1.06E-2	50	6.00E+6	5.70	6.81E+09	6.02E+10	3.88E+4	0.006
15	1.6E+17	1.06E-2	100	2.40E+7	2.70	3.56E+10	4.27E+11	9.61E+4	0.004
16	1.6E+17	1.06E-2	200	9.59E+7	1.35	2.40E+11	2.23E+12	3.24E+5	0.003

TABLE I. Initial conditions (same as Table II of Awe *et al.*⁷) and summary of HELIOS-CR argon simulation results for the indicated quantities, using LTE tabular EOS data. The results are for the computational zone that is initially 1.0 mm inside the inner edge of the liner. All cases have initial liner inner radius of 24.1 cm, liner thickness of 25.5 cm, and temperature of 1.0 eV.

Run	τ_{stag} (μ s)	P_{stag} (Pa)	P_{max} (Pa)	$P_{stag}\tau_{stag}$	$P_{stag}\tau_{stag}/KE_0$
1	8.82	2.37E+08	3.17E+9	2.09E+3	0.09
2	4.51	3.11E+09	8.58E+10	1.40E+4	0.15
3	2.29	3.43E+10	8.82E+11	7.84E+4	0.21
4	1.03	6.29E+11	4.26E+13	6.48E+5	0.43
5	8.84	4.78E+08	4.41E+09	4.23E+3	0.05
6	4.56	6.79E+09	1.32E+11	3.09E+4	0.08
7	2.33	8.39E+10	2.40E+12	1.95E+5	0.13
8	1.19	8.32E+11	2.35E+13	9.86E+5	0.16

TABLE II. RAVEN argon simulation results using a polytropic EOS ($\gamma = 1.6667$) for runs 1–8 of Table I (reproduced from Table II of Awe *et al.*⁷). The results are for the computational zone that is initially 1.0 mm inside the inner edge of the liner.

Run	τ_{stag} (μ s)	P_{stag} (Pa)	P_{max} (Pa)	$P_{stag}\tau_{stag}$	$P_{stag}\tau_{stag}/KE_0$
1	10.30	1.73E+08	7.44E+08	1.79E+3	0.08
2	5.05	1.87E+09	1.09E+10	9.44E+3	0.10
3	2.55	1.63E+10	5.15E+10	4.16E+4	0.11
4	1.30	1.78E+11	3.19E+11	2.32E+5	0.15
5	11.15	3.91E+08	1.64E+09	4.36E+3	0.05
6	5.05	4.11E+09	2.71E+10	2.08E+4	0.06
7	2.65	7.09E+10	1.54E+11	1.88E+5	0.13
8	1.30	3.86E+11	7.70E+11	5.02E+5	0.08

TABLE III. HELIOS-CR argon simulation results using a polytropic EOS ($\gamma = 1.6667$) for runs 1–8 of Table I, for benchmarking against the results of Awe *et al.*⁷ The results are for the computational zone that is initially 1.0 mm inside the inner edge of the liner.

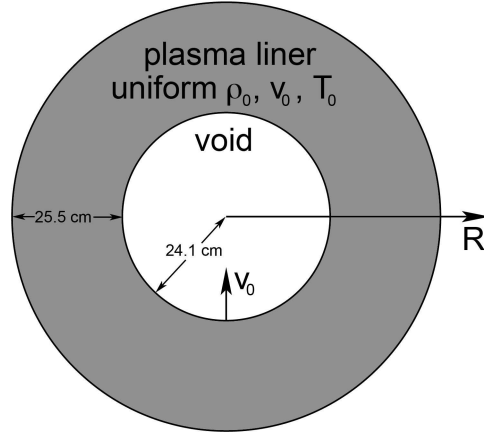


FIG. 1. Schematic of the plasma liner initial conditions used in all simulations. The initial liner mass densities ρ_0 and velocities v_0 are given in Table I. The initial liner temperature $T_0 = T_i = T_e$ is 1.0 eV.

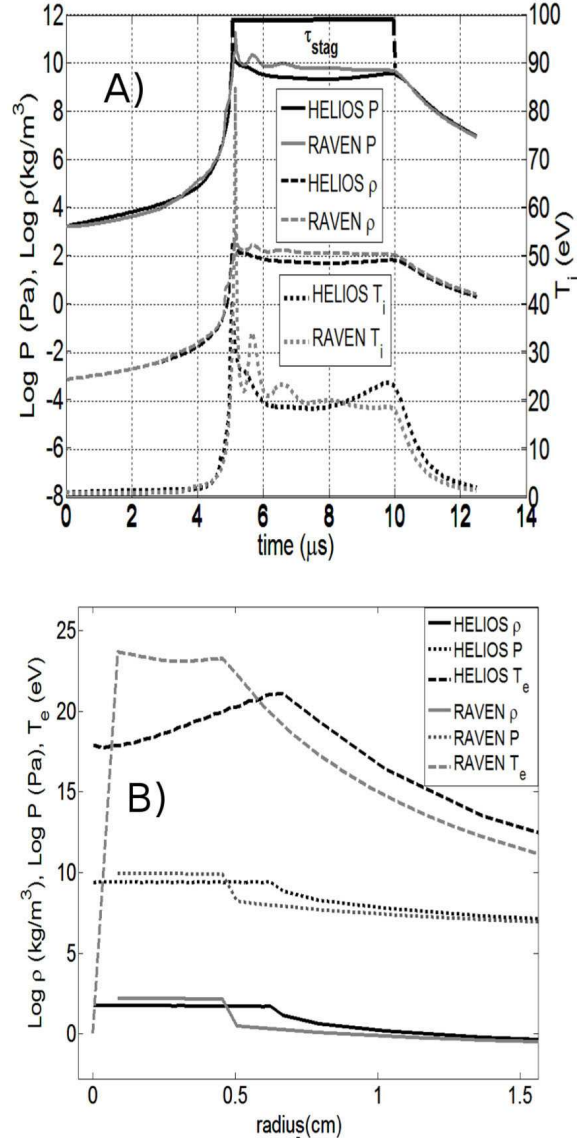


FIG. 2. Benchmarking comparisons of (A) pressure P , mass density ρ , and ion temperature T_i (in the computational zone initially 1.0 cm from the inner edge of the liner) versus time; and (B) P , ρ , and electron temperature T_e versus radius at $t = 6.5 \mu\text{s}$ between RAVEN and HELIOS-CR argon polytropic EOS simulation results of run 6 of Table I.

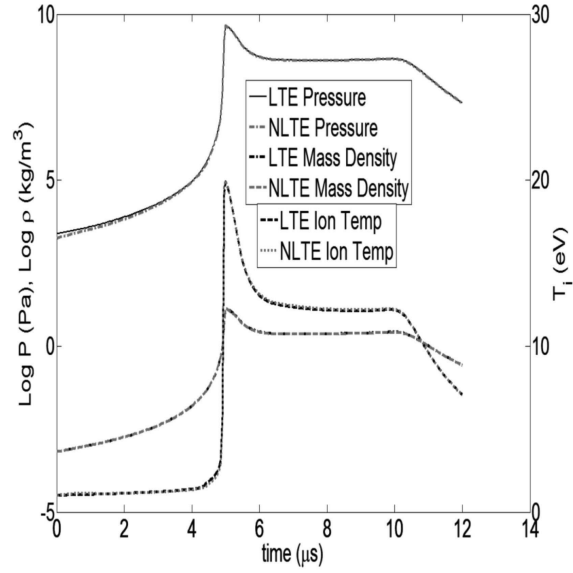


FIG. 3. Comparison of pressure P , mass density ρ , and ion temperature T_i (in the computational zone that is initially 1.0 cm inside the inner edge of the liner) versus time between LTE and non-LTE argon simulation results for run 6 of Table I.

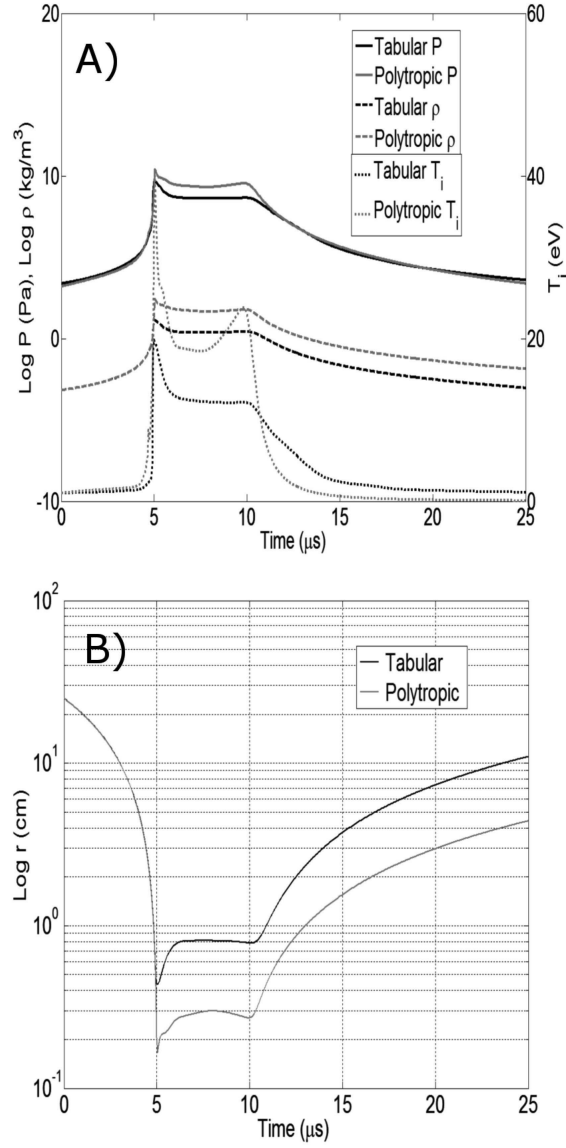


FIG. 4. Comparison between argon LTE tabular EOS and polytropic EOS simulation results for run 6 of Table I for the time evolution of (A) pressure P and ion temperature T_i , and (B) radial position of the liner, for the computational zone that is 1.0 cm from the inside edge of the liner.

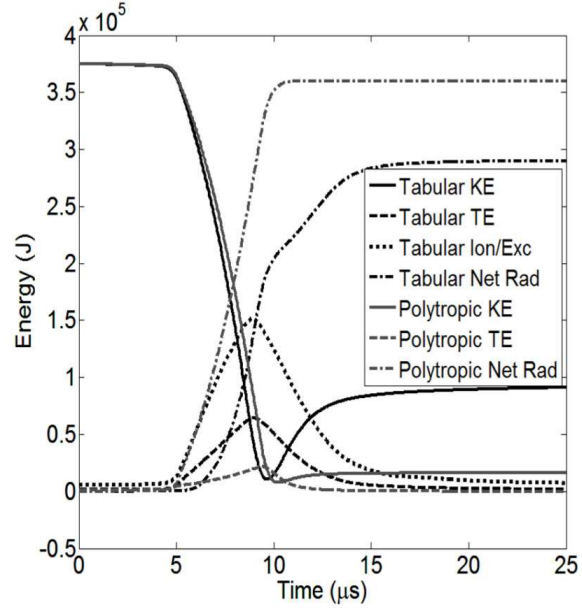


FIG. 5. Comparisons of the instantaneous total liner kinetic (KE), thermal (TE), ionization/excitation, and time-integrated radiated energies of run 6 of Table I using argon tabular LTE and polytropic EOS models. The latter does not include ionization/excitation.

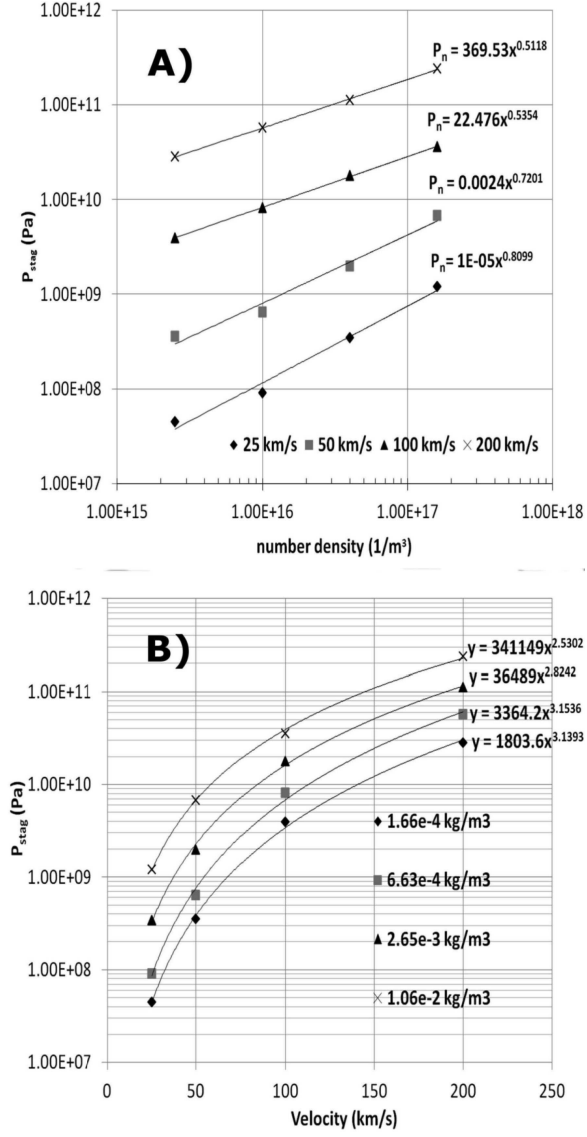


FIG. 6. P_{stag} versus (A) n_o and (B) v_o for the argon runs in Table I, and corresponding power law fits.

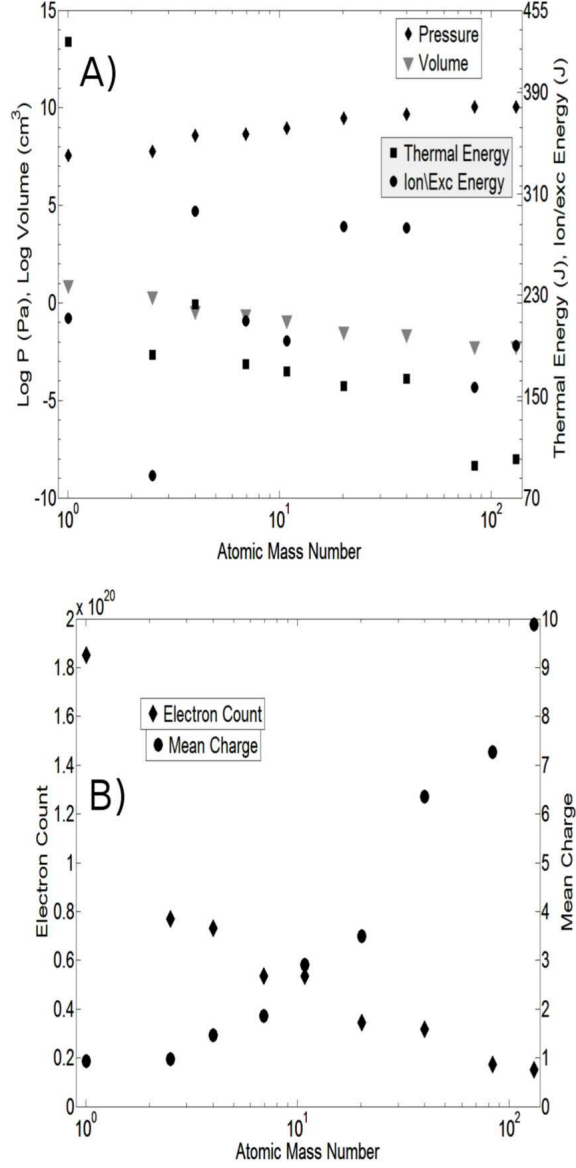


FIG. 7. (A) Pressure, volume, thermal energy, and ionization/excitation energy, and (B) total electron count and mean charge versus liner atomic mass number at the time of peak compression, for the computational zone initially 1.0 cm from the inner edge of the liner, and for initial liner v_0 and ρ_0 corresponding to run 6 of Table I. Liner species (from left to right on plot) include H, D-T, ^4He , ^6Li , ^{11}B , Ne, Ar, Kr, and Xe.